RSC Advances

PAPER

View Article Online
View Journal | View Issue

Cite this: *RSC Adv.*, 2026, **16**, 28634

1,3,2-Dioxaborine-based mero-polyanionic dyes: high-extinction NIR-absorbing polymethines

Vladyslav Polishchuk, * Svitlana Shishkina and Mykola Shandura

Polymethine dyes incorporating multiple *meso*-cyano-2,2-difluoro-1,3,2-dioxaborine units as integral components of the π-chain and 1,3,3-trimethyl-2*H*-indole moieties as donor end-groups were synthesized and characterized. The obtained dyes exhibit an unusual electronic structure that combines merocyanine-like (D–π–A) and polyanionic ([A–π–A′]$_n$) π-conjugated systems within a single mero-polyanionic chromophore, realized in both symmetric (D–π–A–π[–A–π]$_n$–D) and unsymmetric (D–π[–A–π]$_m$–A) architectures. The molecular structures of representative monoanionic dyes from both series were elucidated by X-ray analysis, suggesting a non-uniform distribution of the electron density along the π-conjugated system. These dyes exhibit NIR absorption extending up to 940 nm, with remarkably high molar absorption coefficients of up to 468 000 M^{-1} cm^{-1} in DMF. The position of the long-wavelength absorption maximum shows only weak solvent dependence. The shortest-wavelength oligomers of the studied dyes are strongly fluorescent compounds, with quantum yields of 0.10–0.16 for emission around at 800 nm, and display photostability comparable to that of classical cyanine dyes such as indotricarbocyanine iodide (HITC) and indocyanine green (ICG).

Received 27th April 2026
Accepted 19th May 2026

DOI: 10.1039/d6ra03597c

rsc.li/rsc-advances

Introduction

Organic small molecules that absorb and emit light in the near-infrared (NIR) spectral region (700–2500 nm) are at the forefront of biomedical research and optoelectronics. The NIR tissue transparency window offers several advantages, such as much lower background autofluorescence and minimal photodamage to biological samples.[1,2] The use of long-wavelength organic dyes in optoelectronics benefits from the fact that nearly 50% of solar irradiation lies within the NIR-I (700–1000 nm) and NIR-II (1000–1700 nm) regions.[3,4] Accordingly, NIR organic dyes have found broad applications in bioimaging,[1,5–9] photodynamic (PDT)[10–12] and photothermal (PTT)[13–16] therapies, as well as in the development of organic light-emitting diodes,[17,18] organic lasers,[19,20] and dye-sensitized solar cells.[21–25] However, shifting the spectral window from the visible to the NIR region is accompanied by enhanced lability of organic compounds and their reduced fluorescence efficiency,[26] rendering the design of new long-wavelength fluorescent dyes ever more challenging and demanding.[27,28]

Polymethine dyes, such as cyanines and merocyanines, stand out among known classes of organic dyes as intensely absorbing (molar absorption coefficients often exceed 200 000 M^{-1} cm^{-1}) and strongly fluorescent compounds.[29–31] Within the broad structural landscape of polymethines, cyanine dyes featuring pentamethine and heptamethine scaffolds arguably hold the greatest promise for potential applications.[32,33] For example, the FDA-approved indocyanine green (ICG) is already widely used for fluorescence-guided surgery and perfusion imaging,[34] which prompted extensive research on the development of ICG-like contrast agents with improved characteristics.[35] Moreover, cyanines are broadly investigated for applications in advanced bioimaging techniques (*e.g.*, dual-mode,[36–38] two-photon imaging[37,39]), PDT,[40,41] PTT,[42] and photovoltaics.[43,44]

The attractiveness of cyanines stems from its high structural tunability, allowing broad range of adjustment of physicochemical properties.[45] A classical design strategy for longer-wavelength cyanines involves extending the π-conjugation, resulting in a ~100 nm red shift of the absorption and emission maxima per vinylene unit. However, extension of the π-conjugated chain increases susceptibility to excited-state *cis–trans* isomerization, which becomes the dominant nonradiative deactivation pathway and drastically reduces the fluorescence quantum yield.[46] To mitigate excited-state photoisomerization and suppress the nonradiative excited-state decay, an effective strategy is to rigidify the chromophore by bridging the π-conjugated chain.[47,48]

Bridging of the π-chain of the polymethine dyes can be achieved by introducing the 2,2-difluoro-1,3,2-dioxaborine ring (dioxaborine) into polymethine chain.[49] The dioxaborine is a relatively strong electron-accepting group and its introduction into a cyanine platform alters the overall electronic structure of the chromophore from the classical positively charged D–π–D type to a merocyanine-like D–π–A–π–D type (Fig. 1).[50]

Institute of Organic Chemistry, National Academy of Sciences of Ukraine, Akademika Kukharya Street 5, Kyiv, 02094, Ukraine. E-mail: vlad3ds@gmail.com

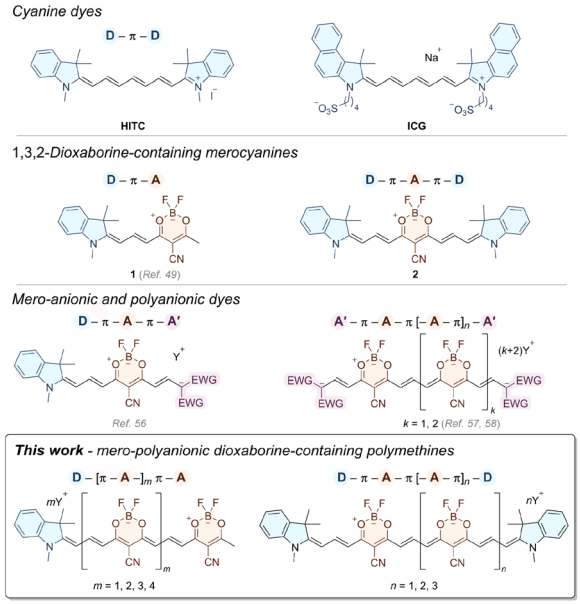

Fig. 1 Cyanine dyes and mero-polyanionic related dioxaborine-containing polymethines.

Remarkably, bridging of the indotricarbocyanine π-chain by the dioxaborine is accompanied by a noticeable increase in fluorescence quantum yields (FQY; from $\Phi_f = 0.19$ for HITC to $\Phi_f = 0.72$ for **2** in dichloromethane (DCM)).[50,51] The dioxaborine-containing polymethines of the D–π–A–π–D and D–π–A types have already been recognized as promising photosensitizers for PDT[52] and fluorogenic probes for biomedical research,[53] especially in the therapy of Alzheimer's disease.[54–56] Accordingly, fusion of the cyanine platform with dioxaborine rings holds great promise as a new strategy toward strongly absorbing and highly fluorescent NIR polymethine dyes.

Previously, we have described the synthesis of 'hybrid' mero-anionic dyes of the D–π–A–π–A′ type[57] and remarkably bright trianionic[58] and tetraanionic[59] polymethines of the A′–π[–A–π]$_n$–A′ type, which contain the 1,3,2-dioxaborine core(s) as an integral part of the π-chain. Herein we report the synthesis and characterization of the long-wavelength mero-polyanionic dyes of symmetric D–π–A–π[–A–π]$_n$–D and unsymmetric D–π[–A–π]$_m$–A types, comprising several dioxaborine rings within a cyanine platform. Sequential addition of the dioxaborine fragments both red-shifts the absorption and emission maxima (up to 940 nm) and endows the resulting mero-polyanionic chromophores with distinctive spectral properties, such as exceptionally high molar absorption coefficients.

Results and discussion

Synthesis

The synthesis of unsymmetric mero-polyanionic dyes (**A**-series) was accomplished starting from anionic precursors **3** and **6** (Scheme 1a).[58] Condensation of **3** with 1,2,3,3-tetramethyl-3*H*-indolium tetrafluoroborate **4** in acetonitrile in the presence of *N*-methylmorpholine (NMM) at room temperature afforded dye **5** in 80% yield. In this reaction, NMM ($pK_a = 7.4$) is the optimal base, as stronger bases promote the self-condensation of **3** to yield a trianionic by-product,[58] whereas weaker bases result in low conversion of the starting materials. Dye **5** was purified by

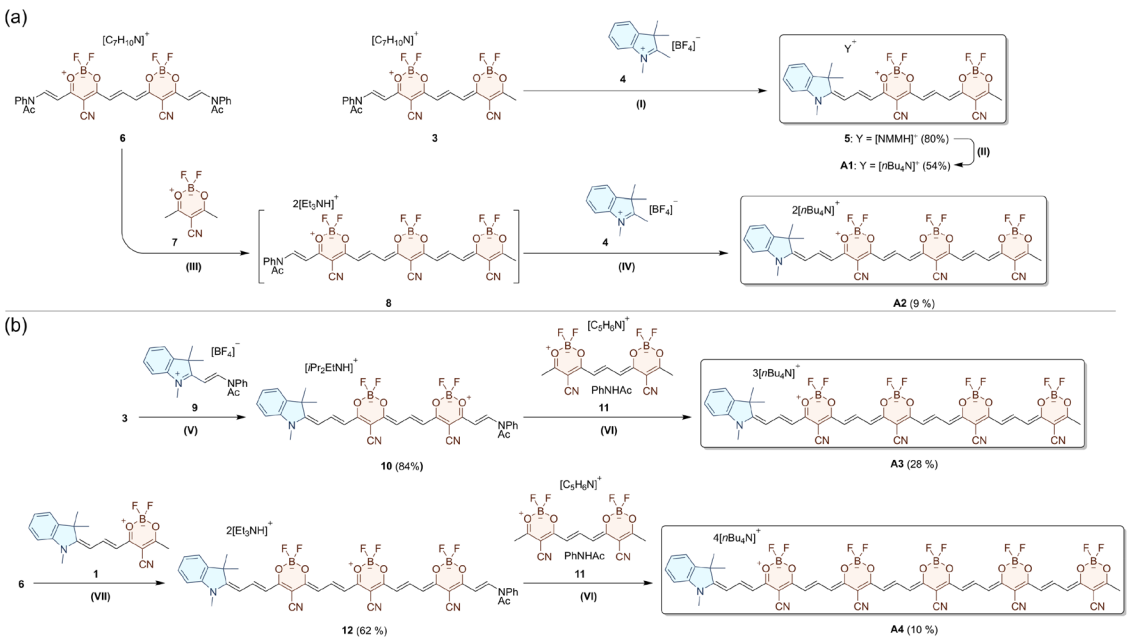

Scheme 1 Synthesis of non-symmetric mero-polyanionic dyes **A1** and **A2** (a) and their longer-wavelength oligomers **A3** and **A4** (b). Reagents and conditions: (I) *N*-methylmorpholine, MeCN, r. t., 16 h; (II) pTLC, then TBAI; (III) Et_3N, MeCN, 30 °C, 15 min.; (IV) (1) Et_3N, MeCN, r. t., 48 h; (2) pTLC, then TBAI; (V) DIPEA, MeCN, r. t., 1 h; (VI) (1) DIPEA, DMF, 40 °C, 16 h; (2) pTLC, then TBAI; (VII) Et_3N, MeCN, r. t., 16 h; $[C_7H_{10}N]^+$ – 2,6-dimethylpyridinium, $[NMMH]^+$ – *N*-methylmorpholin-4-ium, $[C_5H_6N]^+$ – pyridinium, TBAI – tetra-*n*-butylammonium iodide.

preparative thin-layer chromatography (pTLC) on silica gel and then subjected to ion exchange with tetra-*n*-butylammonium iodide to afford the spectrally pure anionic dye **A1**. For the synthesis of the next compound in the **A**-series, dye **A2**, intermediate **8** was first prepared by condensation of **6** with dioxaborine **7** in acetonitrile in the presence of triethylamine. The formation of **8** was monitored by UV-vis-NIR spectroscopy. Subsequently, salt **4** and an additional portion of triethylamine were added to the reaction mixture to furnish the target product. This crude product was purified by pTLC and converted into the tetra-*n*-butylammonium salt of analytically pure **A2**. Despite structural similarity dianionic oligomer **8** is less reactive than monoanionic **3**. Its condensation with **4** thus required a stronger base (DIPEA, $pK_a = 10.8$, *vs.* NMM) and an extended reaction time (48 h *vs.* 16 h) to reach completion. Condensation of **3** with hemicyanine **9** in acetonitrile in the presence of DIPEA afforded monoanionic intermediate **10** in 84% yield, while reaction of symmetric precursor **6** with merocyanine **1** yielded dianionic intermediate **12** in 62% yield (Scheme 1b). Subsequent condensations of intermediates **10** and **12** with anionic dioxaborine **11** in *N*,*N*-dimethylformamide (DMF) in the presence of DIPEA at 40 °C afforded trianionic **A3** and tetraanionic **A4** dyes, respectively.

Symmetric polyanionic dyes (**B**-series) were synthesized in one step starting from compounds **5** and **10** (Scheme 2). For example, reaction of **5** with hemicyanine **9** in acetonitrile in the presence of triethylamine furnished crude **B1**, which was subsequently purified by pTLC and converted to the tetra-*n*-butylammonium salt. The extended **B**-oligomers **B2** and **B3** were synthesized by coupling intermediate **10** with dyes **1** and **5**, respectively. Owing to the substantially diminished reactivity of the methyl group in anionic dye **5** compared to that in merocyanine **1**, the reaction between **5** and **10** proceeds more slowly than between **1** and **10**, requiring elevated temperatures and an extended reaction time to achieve completion.

Ion exchange between crude trialkylammonium salts of the target dyes and tetra-*n*-butylammonium iodide serves two main purposes: additional purification and conversion of the dyes into the more stable tetraalkylammonium salts, as polyanionic dyes with tetraalkylammonium counterions have been reported to exhibit higher stability than those containing trialkylammonium counterions.[58] Moreover, the tetraalkylammonium salts of the mero-polyanionic dyes gave suitable crystals for the X-ray diffraction analysis.

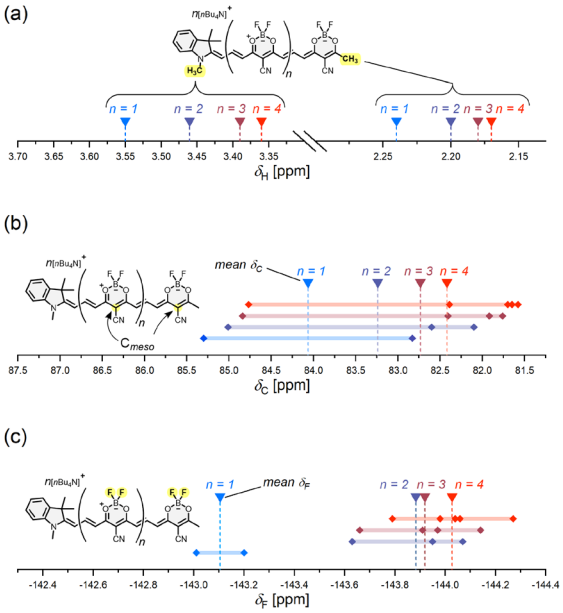

Fig. 2 (a) Characteristic ^{1}H NMR chemical shifts for the indole and dioxaborine end-groups of dyes **A1**–**A4**. (b and c) Variations of the characteristic fluorine (^{11}B–^{19}F) and carbon (C_{meso}) chemical shifts in the **A** series. Data were acquired in DMSO-d_6 as the solvent.

NMR analysis

The spin–spin coupling constants ($^{3}J_{HH}$) between vicinal H-atoms in the π-chain of the studied dyes fall in range of 12–14 Hz, indicating an all-*trans* configuration in solution. In both the **A** and **B** series, the δ_H value of the N–CH_3 protons of the indole end-group(s) (D) gradually shifts upfield in the following order: **A1** – **A2** – **A3** – **A4** and **B1** – **B2** – **B3** (Fig. 2a). An upfield shift of a slightly lower magnitude is also observed for the methyl protons of the dioxaborine end-group (A′) in the **A** series.

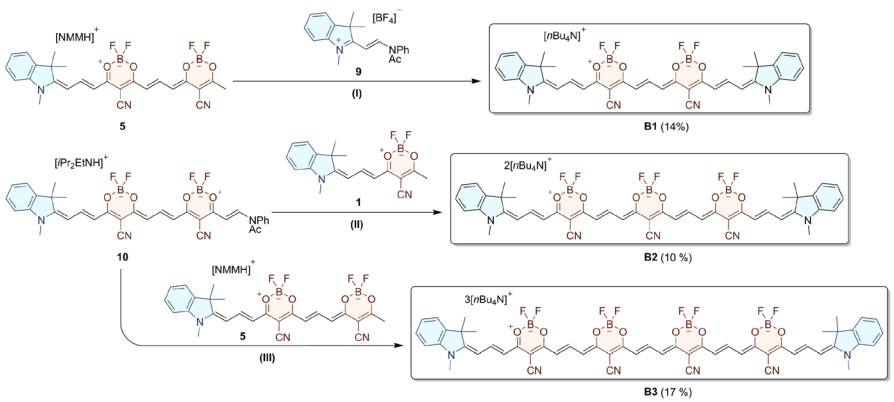

Scheme 2 Synthesis of symmetric mero-polyanionic dyes. Reagents and conditions: (I) (1) Et_3N, MeCN, 40 °C, 1 h; (2) pTLC, then TBAI; (II) (1) Et_3N, DMF, r. t., 1 h; (2) pTLC, then TBAI; (III) (1) DIPEA, DMF, 40 °C, 48 h; (2) pTLC, then TBAI.

These variations in δ_H are not linear, as the additive effect progressively weakens along the series. When considering the arithmetic means of the $\delta_C(C_{meso})$ and $\delta_F(^{11}B–^{19}F)$ values, the similar trend is evident, namely, an overall upfield shift of the $\delta_C(C_{meso})$ and $\delta_F(^{11}B–^{19}F)$ for longer oligomers (Fig. 2b and c).

Given that the local chemical environment of the *meso*-carbons, fluorines ($^{11}B–^{19}F$), and protons (CH_3) is not significantly affected within the both series of dyes from **1** to **4**, their magnetic environment may indeed be slightly altered, as the incorporation of additional dioxaborine units is accompanied by an increase in negative charge within the—albeit more extended—π-conjugated system. Atoms that are spatially adjacent to a negatively charged π-cloud may thus experience stronger shielding in trianionic or tetraanionic chromophore than in monoanionic, reflected in upfield chemical shifts.

X-ray crystal data

Dyes **A1** and **B1** were fully characterized by single-crystal X-ray diffraction, providing a detailed account of their solid-state molecular structure and spatial arrangements (Fig. 3; SI). In agreement with the ^{1}H NMR data in solution, the polymethine chains of their chromophores exhibit the all-*trans* configuration in the crystal. The conjugated π-systems of the both dyes are not completely planar, featuring a slight wave-like bend along the polymethine chain from one end-group to the other. As is characteristic for dioxaborine-containing polymethines, the dioxaborine rings adopt a sofa conformation, in which the boron atoms **B1** and **B2** deviate from the mean plane of the remaining ring atoms to opposite sides of the main chromophore plane **B1** and **B2** are displaced by 0.47 and −0.11 Å, respectively, in **A1** and by −0.45 and 0.40 Å, respectively, in **B1** (Fig. S4 and S6). The unsymmetric dye **A1** is characterized by a small bond-length alternation (BLA) along the polymethine chain, reaching 0.015(7) Å for the π-chain segment linking the indole and dioxaborine units and 0.027(7) Å for the segment connecting two dioxaborine moieties. In the symmetric dye **B1**, much lower BLA is manifested for the central π-chain segment (0.009(3) Å) than for the lateral segments (0.027(4) and 0.046(4) Å). Variations in BLA among different segments of the π-chain in **A1** and **B1** may be indicative of a slightly non-uniform electron distribution in their chromophores. In particular, the central π-chain segment in **B1** displays the most uniform π-electron delocalization.[61]

The crystal structure of dyes **A1** and **B1** is apparently influenced by electrostatic interaction between the negatively charged chromophores and positively charged bulky counterions. The packing of **A1** features a brickwork-like motif of dye anions; the intervening counter-ions preclude the development of extended π–π stacking (Fig. 3c and S5). Proximal chromophores exhibit only minor overlap *via* the dioxaborine end-groups, which are separated by *ca.* 4.3 Å. By contrast, in **B1**, adjacent dye anions form stacked centrosymmetric π–π dimers, enabling maximal stabilizing electrostatic interactions between the alternating positive and negative charges in their chromophores (Fig. 3f and S7). The pronounced π-stacking interactions within the crystal of **B1** are manifested by the remarkably tight packing of adjacent chromophores, with an interplanar separation of only *ca.* 3.1 Å (Fig. 3d).

Photophysical properties

The obtained polyanionic dyes absorb and emit light in a far-red and NIR regions, their absorption (λ_a) and fluorescence (λ_f)

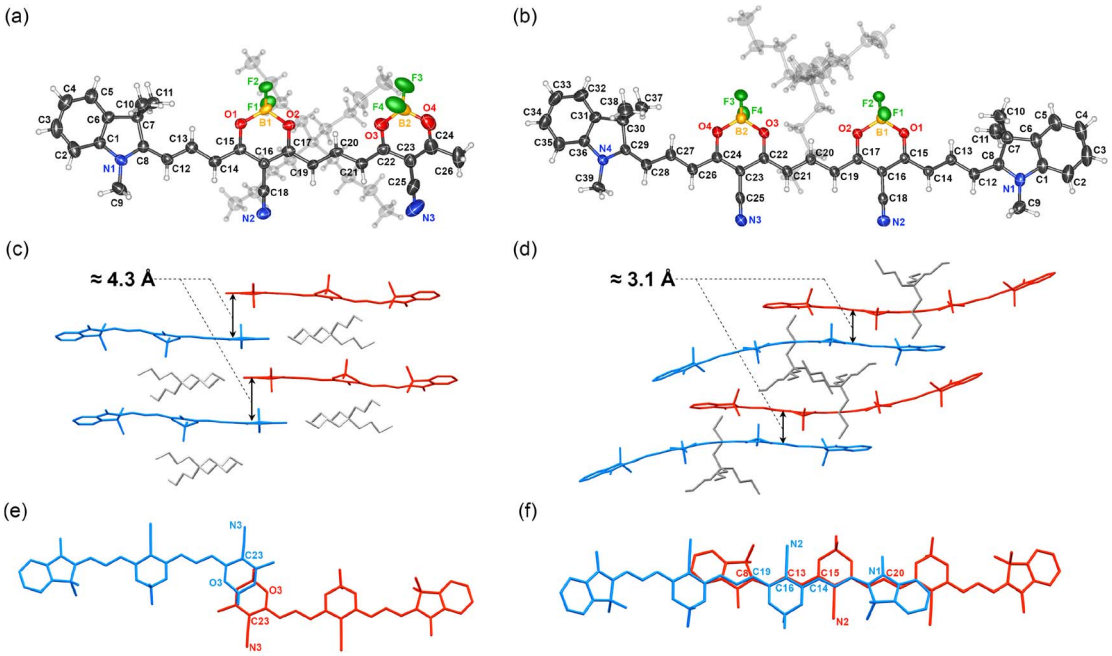

Fig. 3 Molecular structures and molecular packing of dyes **A1** (a, c and e) and **B1** (b, d and f) according to the X-ray diffraction data; thermal ellipsoids are shown at 50% probability level.

Table 1 Spectral parameters of polyanionic dyes A1–A4 and B1–B3

Dye	Solvent	λ_a[a] [nm]	$\varepsilon \times 10^{-5}$[b] [$M^{-1}$ cm^{-1}]	$FWHM_a$[c] [cm^{-1}]	λ_f[d] [nm]	Φ_f[e]	$\Delta\nu_S$[f] [cm^{-1}]	$\varepsilon \cdot \Phi_f \times 10^{-5}$[g] [$M^{-1}$ cm^{-1}]
A1	DCM	655	2.15 ± 0.03	1105	681	0.59 ± 0.03	580	1.27
	MeOH	647	2.10 ± 0.03	1330	683	0.060 ± 0.004	815	0.13
	DMF	664	2.35 ± 0.03	1080	691	0.071 ± 0.004	590	0.17
A2	DCM	765	3.01 ± 0.04	910	795	0.11 ± 0.1	490	0.33
	MeOH	748	—[h]	1160	789	0.017 ± 0.002	695	—
	DMF	767	3.13 ± 0.04	870	795	0.018 ± 0.002	460	0.056
A3	DCM	853	3.54 ± 0.05	1740	880	0.010 ± 0.001	360	0.035
	MeOH	829	—[h]	1840	863	<0.01	475	—
	DMF	847	3.52 ± 0.05	860	873	<0.01	350	—
A4	DCM	921	3.21 ± 0.04	1820	952	<0.01	350	—
	MeOH	895	—[h]	2000	934	<0.01	470	—
	DMF	912	4.25 ± 0.04	800	942	<0.01	350	—
B1	DCM	769	3.43 ± 0.04	970	798	0.16 ± 0.1	470	0.55
	MeOH	761	3.45 ± 0.04	1040	806	0.043 ± 0.003	735	0.15
	DMF	780	3.80 ± 0.05	850	809	0.067 ± 0.004	460	0.25
B2	DCM	854	3.24 ± 0.04	1780	884	0.014 ± 0.001	400	0.045
	MeOH	839	—[h]	1830	874	<0.01	480	—
	DMF	857	3.73 ± 0.05	860	885	0.010 ± 0.001	370	0.037
B3	DCM	924	3.91 ± 0.05	1690	957	<0.01	370	—
	MeOH	902	—[h]	1850	940	<0.01	450	—
	DMF	919	4.68 ± 0.06	810	950	<0.01	355	—

[a] Long-wavelength absorption maximum. [b] Molar absorption coefficient. [c] Full width at half maximum. [d] Emission maximum. [e] Fluorescence quantum yield. [f] Stokes shift. [g] Fluorescence brightness. [h] Dyes **A2**, **A3**, **A4**, **B2**, and **B3** are not soluble enough in MeOH to obtain reliable values of molar absorption coefficient.

maxima ranging from 647 to 924 nm and from 681 to 957 nm, respectively (Table 1). Upon lengthening the π-conjugated system by one dioxaborine-containing unit [–A–π] in the **A**-series from dye **A1** to **A2**, the long-wavelength absorption maximum shifts bathochromically by 110 nm in dichloromethane (DCM). Further elongation of the chromophore results in an attenuated bathochromic effect of λ_a: in the **A2** – **A3** – **A4** sequence, the $\Delta\lambda_a$ amounts to 88 nm and 68 nm in DCM, respectively, reaching λ_a = 921 nm for **A4**. The chromophore extension in the **B1** – **B2** – **B3** sequence is accompanied by similar bathochromic shift as in the **A2** – **A3** –**A4** sequence ($\Delta\lambda_a$ = 85 nm for **B1** to **B2** and $\Delta\lambda_a$ = 70 nm for **B2** to **B3** in DCM).

Both the symmetric (**B1–B3**) and unsymmetric (**A1–A4**) dyes display only marginal solvatochromism, although several distinct trends are evident. Thus, upon going from polar non-protogenic DMF to polar protogenic methanol, the absorption maximum shifts hypsochromically by 17–19 nm (208–385 cm^{-1}) for all studied dyes. However, when going from DCM to MeOH as the solvent, the hypsochromic shift of λ_a progressively increases within the both **A** and **B** series from **A1** (**B1**) to **A4** (**B3**); for example, it ranges from $\Delta\lambda_a$ = 8 nm (189 cm^{-1}) for **A1** to $\Delta\lambda_a$ = 26 nm (315 cm^{-1}) for **A4** (Fig. 4a). Also, in the pair of non-protogenic DCM and DMF, the sign of solvatochromism changes with the chromophore lengthening from **A1** (**B1**) to **A4** (**B3**); for example, for **A1**, the increase of solvent polarity (DCM → DMF) results in a bathochromic shift of the absorption maximum ($\Delta\lambda_a$ = +9 nm), while for **A4** the hypsochromic shift is observed for the same solvent pair ($\Delta\lambda_a$ = −9 nm).

Tetraanionic **A4** and trianionic **B3** dyes exhibit exceptionally high molar absorption coefficients (ε), reaching the values of 425 000 M^{-1} cm^{-1} and 468 000 M^{-1} cm^{-1} (in DMF), respectively (Fig. 4b and c). The molar absorptivities of dyes **A3**, **A2**, and **B2** are also very high, exceeding 300 000 M^{-1} cm^{-1} in both DMF and DCM. Within the **A** series, the molar absorption increases progressively from **A1** to **A4** in DMF; however, in DCM this trend terminates at **A3**, as **A4** exhibits lower ε than **A3** (321 000 *vs.* 354 000 M^{-1} cm^{-1}). Non-linear absorption enhancement is also characteristic of the **B** series in both DMF and DCM, as dianionic dye **B2** exhibits slightly lower ε values than the monoanionic **B1**. The shape of the absorption bands of all studied dyes is typical of cyanine-like polymethines, featuring an intense and narrow long-wavelength band along with a higher-energy (blue-shifted by 1000–1300 cm^{-1} from the long-wavelength peak) vibronic shoulder of more than twofold lower intensity. In addition, similarly to long-wavelength classical cyanines, progressive lengthening of the π-conjugated system of the studied dyes results in a gradual increase of the vibronic shoulder relative intensity (Fig. 4). The studied dyes show no changes in their absorption spectra over the concentration range of 0.05–5 μM, thus excluding aggregate formation in the selected solvents (DCM, MeOH, DMF; Fig. S10 and S11).

The brightest fluorescence of the studied dyes is observed in DCM, whereas in MeOH and DMF the emission intensity is much lower. For example, the fluorescence quantum yields (FQY, Φ_f) of the monoanionic dyes **A1** and **B1** reach 0.59 and 0.16 in DCM, respectively; which are relatively high values as for NIR-emitting dyes of the polymethine family. However, in MeOH and DMF, the FQYs do not exceed 0.1 for both **A1** and **B1**, while for their higher oligomers (**A3**, **A4**, **B2**, and **B3**) fluorescence is barely detectable in polar media. In general, within both the **A** and **B** series, the fluorescence intensity decreases from **A1** (**B1**) to **A4** (**B3**), consistent for long-wavelength

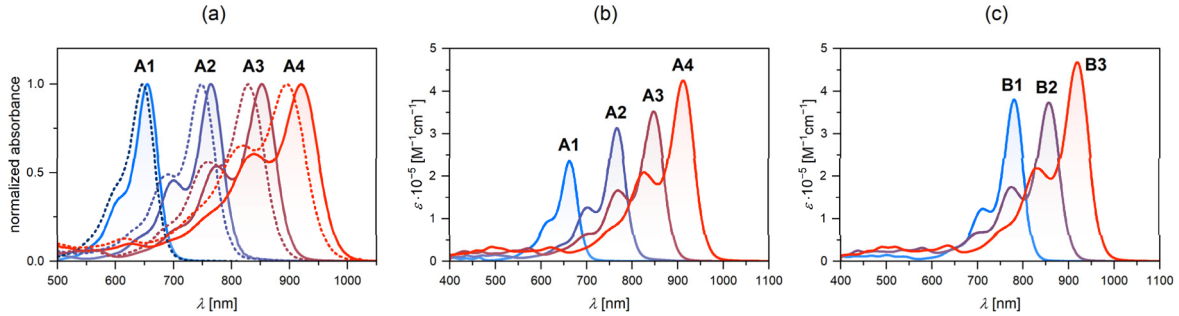

Fig. 4 (a) Normalized absorption spectra of dyes **A1**–**A4** in DCM (solid lines) and in MeOH (dotted lines). Absorption spectra of dyes **A1**–**A4** (b) and **B1**–**B3** (c) in DMF.

polymethines from the energy gap law (enhanced internal conversion)[62] and the increasing propensity for excited-state photoisomerization,[63] which promotes non-radiative deactivation. The Stokes shifts ($\Delta\nu_S$) of all studied dyes fall in the range of 26–45 nm (350–810 cm^{-1}) and are scarcely influenced by solvent polarity, though they are generally higher in MeOH than in DCM or DMF (Table 1). Note that, while the optical properties of the studied dyes differ only slightly in DCM and DMF, there are more pronounced changes when going to protogenic MeOH: increased hypsochromic shifts and $\Delta\nu_S$ values, as well as broader absorption bands. Given the anionic nature of the studied dyes, these effects may be explained by stronger electrophilic solvation of their chromophores by the protogenic solvent.

Stability

The synthesized polyanionic dyes are stable in the solid state, while their stability in solution is dependent on the solvent nature. For example, in non-protogenic DCM, all dyes showed no discernible degradation at concentrations 0.5–1.0 × 10^{-5} mol L^{-1} after a week of storage in the darkness. At that, they are highly sensitive to trace amounts of acids in solution. This effect is particularly pronounced in non-stabilized, partially degraded DCM, and manifested in drastic decrease of the molar absorptivity and broadening of the absorption band. Still, the original band shape can be restored by neutralizing excess acid with bases. The dyes are as stable in DMF as in DCM, showing only minor (≤5%) decrease in absorption intensity after one week storage in the dark. By contrast, their stability in protogenic MeOH is significantly impaired. For example, in MeOH the absorption intensity of dye **A1** decreases by 12% after 24 h of storage in the dark, whereas the long-wavelength band of **A4** almost completely disappears after several days under the same conditions.

The relative stabilities of all obtained dyes were evaluated against the classical cyanines HITC and ICG under controlled conditions. Photodegradation was assessed by comparing absorption intensities before and after 30 min irradiation of dye solutions in MeCN with UV light (λ_{ex} = 300 nm). The results show that in the HITC/ICG pair, the former is more photostable: after 30 min under the experimental conditions, the absorption of HITC decreased by 7%, whereas that of ICG decreased by 43% (Fig. S12). Dyes absorbing in the 650–750 nm region (**A1**, **A2**, and **B1**) exhibit photostability comparable to HITC (λ_a = 740 nm in MeCN), whereas longer-wavelength dyes **A3**, **A4**, **B2**, and **B3**, absorbing in the 850–920 nm range, are comparable to ICG (λ_a = 784 nm in MeCN). As the π-conjugated system is extended by additional dioxaborine units, photostability decreases linearly in both the **A** and **B** series (Fig. S13).

The possible mechanism of light-induced photodegradation involves a photooxidation pathway, in which the photoexcited dye interacts with oxygen to generate reactive oxygen species (ROS). Subsequent reactions of the dyes with ROS lead to their degradation, producing byproducts such as 1-alkyl-3,3-trimethylindolin-2-one and derivatives of Fischer's aldehyde.[64] When the experiments were performed under oxygen-free conditions (by bubbling argon through the dye solutions for 10 min), photodegradation under 300 nm irradiation was significantly reduced. For example, under these conditions **B3** degraded by only 11% (*vs.* 59% in non-degassed MeCN), while **A4** degraded by 7% (*vs.* 43% in non-degassed MeCN; Fig. S14). These results indicate that the primary bleaching pathway of the mero-polyanionic dyes is oxygen-dependent, which consistent with the typical degradation behaviour of cyanine dyes.

Conclusions

In summary, we report the synthesis and characterization of new mero-polyanionic polymethines of D–π–A–π[–A–π]$_n$–D and D–π[–A–π]$_m$–A types incorporating *meso*-cyano-substituted 1,3,2-dioxaborine units (**A**) and 1,3,3-trimethyl-2*H*-indole end-groups (D). Both symmetric (**B** series) and unsymmetric (**A** series) dyes with monoanionic (n, m = 1), dianionic (n, m = 2), trianionic (n, m = 3), and tetraanionic (m = 4) chromophore structures were synthesized. The molecular structures of monoanionic oligomers of symmetric and unsymmetric dyes were ascertained by X-ray diffraction analysis. In the solid state, the dyes exhibit a non-uniform π-electron distribution, as evident by variations in BLA exhibit across different segments of the π-chain. Stepwise incorporation of dioxaborine-containing [–A–π] units induces bathochromic shifts of the long-wavelength absorption maximum, reaching λ_a = 924 nm for trianionic symmetric and λ_a = 921 nm for tetraanionic unsymmetric dyes in DCM. All dyes exhibit high molar

absorption coefficients in DCM and DMF, up to 391 000 M^{-1} cm^{-1} in DCM and 468 000 M^{-1} cm^{-1} in DMF. Fluorescence quantum yields are highest for the mono- and dianionic oligomers (0.11–0.59 in DCM), whereas in DMF and MeOH all dyes are weakly fluorescent. The dyes display negligible solvatochromism, minimal fluorochromic behaviour, and small Stokes shifts. As the absorption shifts to longer-wavelengths, photostability decreases linearly in both series, although it remains comparable to that of classical cyanines (HITC and ICG) operating in the same spectral region.

Experimental section

The studied mero-polyanionic dyes were synthesized according to the procedures provided in the SI. Commercially available spectral grade DCM, methanol, and *N*,*N*-dimethylformamide (DMF) were used as the solvents for spectral measurements without further purification. The ^{1}H NMR (300 MHz or 400 MHz), ^{19}F NMR (188 MHz, $CFCl_3$ as an external standard), and ^{13}C NMR (76 MHz) spectra were recorded on Varian VXR-300 or Varian Unity-400 spectrometers. The residual solvent peaks of DMSO-d_6 ($\delta_H = 2.50$ ppm, $\delta_C = 39.51$ ppm) were used as internal standards. The following abbreviations are used to denote NMR peak multiplicities: s = singlet, d = doublet, t = triplet, q = quartet, quint = quintet, sxt = sextet, m = multiplet, br = broad. Original NMR spectra are provided in the SI.

Single crystals of dyes **A1** and **B1** suitable for X-ray diffraction analysis were obtained by slow evaporation from EtOAc/acetone (1 : 1) solutions. Detailed crystallographic data are provided in the SI. Supplementary crystallographic data for this paper are available under deposition numbers 2548387 (compound **A1**) and 2548388 (compound **B1**). These data can be obtained free of charge from the joint Cambridge Crystallographic Data Centre and Fachinformationszentrum Karlsruhe Access Structures service.

The UV-vis-NIR absorption and fluorescence spectra were measured using a Shimadzu UV-3100 spectrophotometer and a Solar CM-2203 spectrofluorometer (modified with a Hamamatsu-S7031 CCD detector for NIR measurements up to 1030 nm), respectively. To minimize the inner filter effects, the optical densities of dye solutions in fluorescence measurements did not exceed 0.1 in the absorption maximum. The fluorescence quantum yields (Φ_f) were determined relative to ICG ($\Phi_R = 0.13$, EtOH) and HIDC ($\Phi_R = 0.28$, EtOH).[60] The values of Φ_f were corrected taking into account refractive indexes of the solvents: $\Phi_f = \Phi_R \times (I/I_R) \times (A_R/A) \times (n^2/n_R^2)$, where Φ_R is the fluorescence quantum yield of the reference dye; I and I_R are the integrated fluorescence intensities of the tested compound and the reference dye, respectively; A and A_R are the optical densities at the excitation wavelength; n and n_R are the refractive indices of the solvents used.

The molar absorption coefficients (ε) were determined according to the Beer–Lambert law by measuring the absorbance of a concentration series for each dye. Solutions were prepared by dissolving precisely weighed amounts of each compound and subsequently diluted to a working concentration range of 0.5–4.0 μM. To ensure the highest accuracy and to exclude the influence of molecular aggregation, the linearity of the absorbance at λ_a *versus* concentration was verified through linear regression analysis. All dyes exhibited a linear correlation, confirming the absence aggregation, scattering, or detector saturation effects within the studied range. Data were collected from four independent measurements using 10 mm quartz cuvettes at 25 °C.

Photostability of dyes **A1–A4**, **B1–B3**, HITC, and ICG was studied under controlled conditions: dye solutions in acetonitrile with optical densities 0.05–0.10 in the absorption maximum were placed in a 1 cm quartz cuvette in the fluorescent spectrometer (Solar CM2203, 250 W xenon lamp as the excitation source). Photodecomposition of the samples was monitored in "kinetics" mode under continuous irradiation for 30 min at 300 nm, by recording the decrease in fluorescence intensity over time. Slit widths of the excitation monochromator were set to the value of 6 mm, which corresponds to 28.5 nm of excitation bandwidth at half maximum. Photostability was also evaluated by comparing the initial and final absorption spectra of the studied solutions. The 300 nm excitation wavelength was chosen for intrinsic photostability assessment between **A1–A4**, **B1–B3**, HITC, and ICG. Under irradiation by 650 nm for 2 h no detectable photodegradation was observed.

Conflicts of interest

There are no conflicts to declare.

Data availability

The data that support the findings of this study are available in the supplementary information (SI) of this paper. Supplementary information is available. See DOI: https://doi.org/10.1039/d6ra03597c.

CCDC 2548387 and 2548388 contain the supplementary crystallographic data for this paper.[65a,b]

Acknowledgements

The authors are grateful to Dr Andrii Kulinich for helpful discussions. The authors thank the National Research Foundation of Ukraine for the opportunity to conduct this study under grant 2025.07/0400 "Electron-vibrational processes in hybrid MXene-based nanosystems" and all the brave defenders of Ukraine who allow us to continue our scientific work.

Notes and references

1 J. V. Frangioni, *Curr. Opin. Chem. Biol.*, 2003, **7**, 626–634.
2 J. Miller, in *Standardization and Quality Assurance in Fluorescence Measurements I*, ed. U. Resch-Genger, Springer Berlin Heidelberg, Berlin, Heidelberg, 2008, pp. 147–162.
3 F. Grifoni, M. Bonomo, W. Naim, N. Barbero, T. Alnasser, I. Dzeba, M. Giordano, A. Tsaturyan, M. Urbani, T. Torres, C. Barolo and F. Sauvage, *Adv. Energy Mater.*, 2021, **11**, 2101598.
4 O. Ostroverkhova, *Chem. Rev.*, 2016, **116**, 13279–13412.

5 G. Hong, A. L. Antaris and H. Dai, *Nat. Biomed. Eng.*, 2017, **1**, 0010.
6 K. Kiyose, H. Kojima and T. Nagano, *Chem.–Asian J.*, 2008, **3**, 506–515.
7 S. Luo, E. Zhang, Y. Su, T. Cheng and C. Shi, *Biomaterials*, 2011, **32**, 7127–7138.
8 G. Qian and Z. Y. Wang, *Chem.–Asian J.*, 2010, **5**, 1006–1029.
9 L. Yuan, W. Lin, K. Zheng, L. He and W. Huang, *Chem. Soc. Rev.*, 2013, **42**, 622–661.
10 H. Abrahamse and M. R. Hamblin, *Biochem. J.*, 2016, **473**, 347–364.
11 V.-N. Nguyen, Y. Yan, J. Zhao and J. Yoon, *Acc. Chem. Res.*, 2021, **54**, 207–220.
12 C. Zhao, T. Du, B. Zhu, Z. He, H.-Y. Wang and Y. Liu, *Coord. Chem. Rev.*, 2025, **544**, 216962.
13 B. Zhou, Y. Li, G. Niu, M. Lan, Q. Jia and Q. Liang, *ACS Appl. Mater. Interfaces*, 2016, **8**, 29899–29905.
14 Y. Chen, L. Li, W. Chen, H. Chen and J. Yin, *Chin. Chem. Lett.*, 2019, **30**, 1353–1360.
15 S. Guo, D. Gu, Y. Yang, J. Tian and X. Chen, *J. Nanobiotechnol.*, 2023, **21**, 348.
16 M. Yang, C. Ji and M. Yin, *Wiley Interdiscip. Rev.:Nanomed. Nanobiotechnol.*, 2024, **16**, e1960.
17 A. Zampetti, A. Minotto and F. Cacialli, *Adv. Funct. Mater.*, 2019, **29**, 1807623.
18 P. L. dos Santos, P. Stachelek, Y. Takeda and P. Pander, *Mater. Chem. Front.*, 2024, **8**, 1731–1766.
19 A. J. C. Kuehne and M. C. Gather, *Chem. Rev.*, 2016, **116**, 12823–12864.
20 J.-J. Wu, X.-D. Wang and L.-S. Liao, *ACS Photonics*, 2019, **6**, 2590–2599.
21 A. Mishra, M. K. R. Fischer and P. Bäuerle, *Angew. Chem., Int. Ed.*, 2009, **48**, 2474–2499.
22 K. H. Hendriks, W. Li, M. M. Wienk and R. A. J. Janssen, *J. Am. Chem. Soc.*, 2014, **136**, 12130–12136.
23 J. W. Jung, J. W. Jo, E. H. Jung and W. H. Jo, *Org. Electron.*, 2016, **31**, 149–170.
24 C. Liu, K. Wang, X. Gong and A. J. Heeger, *Chem. Soc. Rev.*, 2016, **45**, 4825–4846.
25 G. Zhang, J. Zhao, P. C. Y. Chow, K. Jiang, J. Zhang, Z. Zhu, J. Zhang, F. Huang and H. Yan, *Chem. Rev.*, 2018, **118**, 3447–3507.
26 R. Englman and J. Jortner, *Mol. Phys.*, 1970, **18**, 145–164.
27 H. Piwoński, S. Nozue and S. Habuchi, *ACS Nanosci. Au*, 2022, **2**, 253–283.
28 C. T. Jackson, S. Jeong, G. F. Dorlhiac and M. P. Landry, *iScience*, 2021, **24**, 102156.
29 A. Mishra, R. K. Behera, P. K. Behera, B. K. Mishra and G. B. Behera, *Chem. Rev.*, 2000, **100**, 1973–2012.
30 A. V. Kulinich and A. A. Ishchenko, *Chem. Rev.*, 2024, **124**, 12086–12144.
31 J. Fabian, H. Nakazumi and M. Matsuoka, *Chem. Rev.*, 1992, **92**(6), 1197–1226.
32 Y. Qiu, B. Yuan, Y. Cao, X. He, O. U. Akakuru, L. Lu, N. Chen, M. Xu, A. Wu and J. Li, *Wiley Interdiscip. Rev.:Nanomed. Nanobiotechnol.*, 2023, **15**, e1910.
33 X. Zhao, Q. Yao, S. Long, W. Chi, Y. Yang, D. Tan, X. Liu, H. Huang, W. Sun, J. Du, J. Fan and X. Peng, *J. Am. Chem. Soc.*, 2021, **143**, 12345–12354.
34 P. Fransvea, M. Miccini, F. Rondelli, G. Brisinda, A. Costa, G. M. Garbarino and G. Costa, *J. Clin. Med.*, 2024, **13**, 4895.
35 A. P. Gorka, R. R. Nani and M. J. Schnermann, *Acc. Chem. Res.*, 2018, **51**, 3226–3235.
36 X. Zou, Y. Zhao and W. Lin, *Anal. Chim. Acta*, 2023, **1239**, 340713.
37 P. Wu, Z. Qu, J. Zhang, X. Ren, D. Wang, C. Huang, K. Cheng, J. Qi, H. Shi, S. Gan, W. Wei, Y. Zhang, C. Lee, L. Wang and H. Sun, *Adv. Funct. Mater.*, 2025, **35**, 2400597.
38 X. Kong, M. Li, B. Dong, N. Zhang, W. Song, Y. Lu and W. Lin, *Analyst*, 2019, **144**, 4371–4379.
39 S. J. J. Kwok, M. Choi, B. Bhayana, X. Zhang, C. Ran and S.-H. Yun, *Sci. Rep.*, 2016, **6**, 23866.
40 C. Shi, J. B. Wu and D. Pan, *J. Biomed. Opt.*, 2016, **21**, 050901.
41 N. Lange, W. Szlasa, J. Saczko and A. Chwiłkowska, *Pharmaceutics*, 2021, **13**, 818.
42 Z. Kejík, J. Hajduch, N. Abramenko, F. Vellieux, K. Veselá, J. L. Fialová, K. Petrláková, K. Kučnirová, R. Kaplánek, A. Tatar, M. Skaličková, M. Masařík, P. Babula, P. Dytrych, D. Hoskovec, P. Martásek and M. Jakubek, *Commun. Chem.*, 2024, **7**, 180.
43 W. Naim, V. Novelli, I. Nikolinakos, N. Barbero, I. Dzeba, F. Grifoni, Y. Ren, T. Alnasser, A. Velardo, R. Borrelli, S. Haacke, S. M. Zakeeruddin, M. Graetzel, C. Barolo and F. Sauvage, *JACS Au*, 2021, **1**, 409–426.
44 W. Ghann, H. Kang, E. Emerson, J. Oh, T. Chavez-Gil, F. Nesbitt, R. Williams and J. Uddin, *Inorg. Chim. Acta*, 2017, **467**, 123–131.
45 J. Yuan, H. Yang, W. Huang, S. Liu, H. Zhang, X. Zhang and X. Peng, *Chem. Soc. Rev.*, 2025, **54**, 341–366.
46 E. M. S. Stennett, M. A. Ciuba and M. Levitus, *Chem. Soc. Rev.*, 2014, **43**, 1057–1075.
47 M. S. Michie, R. Götz, C. Franke, M. Bowler, N. Kumari, V. Magidson, M. Levitus, J. Loncarek, M. Sauer and M. J. Schnermann, *J. Am. Chem. Soc.*, 2017, **139**, 12406–12409.
48 S. S. Matikonda, G. Hammersley, N. Kumari, L. Grabenhorst, V. Glembockyte, P. Tinnefeld, J. Ivanic, M. Levitus and M. J. Schnermann, *J. Org. Chem.*, 2020, **85**, 5907–5915.
49 P.-Z. Chen, L.-Y. Niu, Y.-Z. Chen and Q.-Z. Yang, *Coord. Chem. Rev.*, 2017, **350**, 196–216.
50 V. Polishchuk, M. Stanko, A. Kulinich and M. Shandura, *Eur. J. Org Chem.*, 2018, **2018**, 240–246.
51 E. S. Voropai, M. P. Samtsov and K. N. Kaplevskii, *J. Appl. Spectrosc.*, 2003, **70**, 721–728.
52 X. Zhao, Y. Yang, Y. Yu, S. Guo, W. Wang and S. Zhu, *Chem. Commun.*, 2019, **55**, 13542–13545.
53 M. Collot, *Mater. Horiz.*, 2021, **8**, 501–514.
54 C. Ran, X. Xu, S. B. Raymond, B. J. Ferrara, K. Neal, B. J. Bacskai, Z. Medarova and A. Moore, *J. Am. Chem. Soc.*, 2009, **131**, 15257–15261.
55 X. Zhang, Y. Tian, Z. Li, X. Tian, H. Sun, H. Liu, A. Moore and C. Ran, *J. Am. Chem. Soc.*, 2013, **135**, 16397–16409.

56 X. Zhang, Y. Tian, P. Yuan, Y. Li, M. A. Yaseen, J. Grutzendler, A. Moore and C. Ran, *Chem. Commun.*, 2014, **50**, 11550–11553.
57 V. Polishchuk, A. Kulinich, S. Suikov, E. Rusanov and M. Shandura, *New J. Chem.*, 2022, **46**, 1273–1285.
58 V. Polishchuk, M. Filatova, E. Rusanov and M. Shandura, *Chem.–Eur. J.*, 2022, **28**, e202202168.
59 V. Polishchuk, A. Kulinich and M. Shandura, *Chem.–Eur. J.*, 2024, **30**, e202401097.
60 K. Rurack and M. Spieles, *Anal. Chem.*, 2011, **83**, 1232–1242.
61 L. M. Tolbert and X. Zhao, *J. Am. Chem. Soc.*, 1997, **119**, 3253–3258.
62 J. V. Caspar and T. J. Meyer, *J. Phys. Chem.*, 1983, **87**(6), 952–957.
63 M. Levitus and S. Ranjit, *Q. Rev. Biophys.*, 2011, **44**, 123–151.
64 R. R. Nani, J. A. Kelley, J. Ivanic and M. J. Schnermann, *Chem. Sci.*, 2015, **6**, 6556–6563.
65 (*a*) CCDC 2548387: Experimental Crystal Structure Determination, 2026, DOI: 10.5517/ccdc.csd.cc2rjt15; (*b*) CCDC 2548388: Experimental Crystal Structure Determination, 2026, DOI: 10.5517/ccdc.csd.cc2rjt26.